Chapter 7
Small-Animal MRI Instrumentation

Andrew M. Blamire

1 Introduction

Magnetic resonance imaging (MRI) emerged in the 1970s from the laboratories of physical scientists where the basic phenomenon of nuclear magnetic resonance (NMR) was being investigated, and has rapidly expanded to permeate most areas of biological and clinical research. MRI is undoubtedly the most versatile of all the non-invasive imaging modalities. The MRI signal originates from the nucleus of the hydrogen atom (the proton) and while the intrinsic contrast of the MRI image reflects differences in proton density within the tissue, selection of appropriate signal preparation schemes allows image intensity to be linked to other important processes such as blood flow (e.g. bulk flow for angiography or micro flow for tissue perfusion), Brownian water motion (e.g. diffusion imaging to assess tissue microstructure), tissue oxygenation (for functional information), etc. Further, the local chemical environment of the nucleus modulates the MRI signal frequency allowing the identification of molecular groups using the allied technique of MRI spectroscopy (MRS) allowing metabolic measurements. No other imaging modality can rival this inherent flexibility. For all of these MRI measurement, the scanning instrumentation remains essentially constant, with selection of the contrast type determined by the specific imaging sequence alone. In this chapter we describe in detail the basic instrumentation required for small animal MRI.

2 Background to Magnetic Resonance

In this section we give a brief overview of the fundamentals of the MRI experiment as a background to describing the design and selection of MRI instrumentation.

A.M. Blamire (✉)
Newcastle Magnetic Resonance Centre, Newcastle University, Newcastle upon Tyne, UK
e-mail: andrew.blamire@newcastle.ac.uk

2.1   The Fundamentals of MRI Signal Generation

A complete description of the MRI experiment is beyond the scope or purpose of this chapter and has been described in many good texts on that subject [1, 2]. However, in order to understand the design criteria and selection of MRI instrumentation it is necessary to first introduce some basic concepts.

MRI is based on the fundamental physical property of some nuclei known as nuclear magnetic resonance (NMR) which was first shown experimentally in 1945, and for which Felix Bloch and Edward Purcell shared the 1952 Nobel Prize for Physics. Key nuclei (e.g. ^1H, ^{13}C, ^{31}P, ^{23}Na, ^{19}F, ^7Li) possess a property described by quantum mechanics as *spin* (which equates well to a classical description of the nucleus rotating on its axis), and which leads to a property called the magnetic moment (μ). (Classically a rotating charged object can be decomposed into a series of circulating charged sub-particles which constitute an electric current, which has an associated magnetic field.) When placed in a strong uniform magnetic field (denoted B_o and by convention aligned along the z axis) these nuclei polarize between several discrete energy levels (the number of which is nucleus specific). In the case of conventional MRI the nucleus of interest is the proton which has two discrete (quantized) energy levels.

The energy separation (ΔE) for a two level system is given by

$$\Delta E = \gamma h B_o / 2\pi \tag{7.1}$$

where γ is a nucleus specific constant known as the magnetogyric ratio and h is Planks constant. In the NMR experiment this energy is imparted to the nuclei via an applied electromagnetic wave of angular frequency ω which has associated energy given by

$$E = h\omega / 2\pi \tag{7.2}$$

For MRI the frequency of this electromagnetic wave is within the radio-frequency (RF) band. For resonant absorption of energy by the nuclei we can equate Eqs. (7.1) and (7.2) to obtain the expression

$$\omega_o = \gamma B_o \tag{7.3}$$

which describes the required RF frequency for nuclear resonance at a given magnetic field strength. This frequency ω_o is known as the *Larmor* frequency.

On a macroscopic scale the effect of polarizing the individual magnetic moments is to create a net *magnetization* along the axis of the magnet. A pulse of RF energy applied to the system causes a rotation of the magnetization vector away from the z axis towards the x–y plane (Fig. 7.1). The precise angle (α) through which the magnetization is rotated is known as the *flip angle* and is determined by the strength of the magnetic component of the applied RF pulse (B_1) and the pulse duration t_p.

$$\alpha = \int_0^{t_p} \gamma B_1(t') \, dt' \tag{7.4}$$
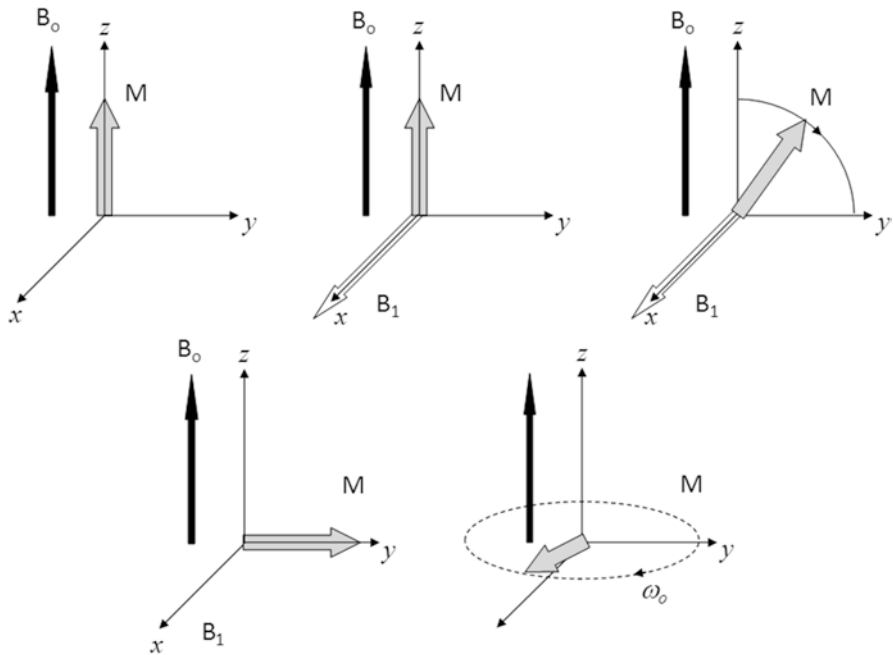
Fig. 7.1 The classical description of the nuclear magnetic resonance (NMR) experiment. In the presence of a polarizing field $B_o(z)$ the sample has a net magnetization M. The magnetic field component (B_{1x}) of an applied pulse of RF energy causes the magnetization to rotate into the transverse (xy) plane. The main field exerts a torque on the transverse magnetization causing it to precess in the xy plane where it can induce a current in a suitably placed receiver coil

The interaction between the main magnetic field and the magnetization component in the x–y plane is a torque which causes the magnetization to precess about the axis of the main field at the Larmor frequency. This precession can be detected by electromagnetic induction in a suitably placed detector coil.

2.2 Properties of the MRI Signal

Once the MRI signal has been excited, two main processes take over to return the nuclei to their equilibrium state. These are known as *relaxation* and act to destroy the observable magnetic resonance signal, and restore the original polarization of the nuclei in the applied magnetic field.

2.2.1 Transverse, T_2 or Spin–Spin Relaxation

Following excitation by an RF pulse the transverse component of magnetization precesses under the action of the main applied magnetic field. At the atomic level fluctuations occur in the local environment of each nucleus due to interactions
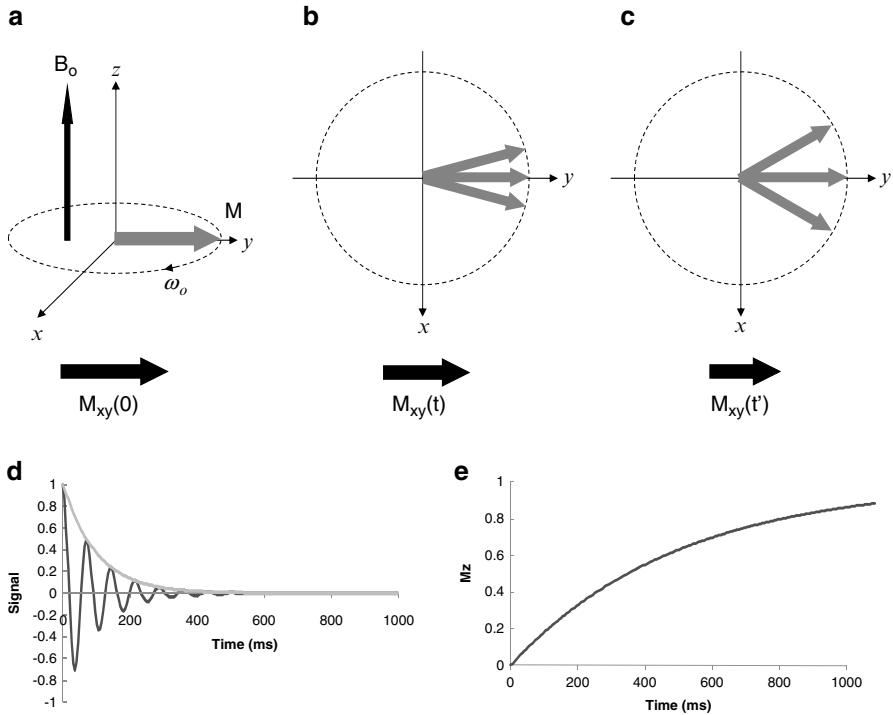
Fig. 7.2 Illustration of the precession of magnetization and relaxation processes. (**a–d**) Interactions between individual nuclei (spin–spin interactions) causes loss of the coherent precession within the net magnetization leading to the decay of the M_{xy} component of magnetization, (**e**) recovery of the longitudinal magnetization M_z due to spin–lattice or T_1 relaxation

between closely located nuclei (termed spin–spin interactions), such that energy is transferred from nuclei to nuclei. These fluctuations cause loss of coherence in the precession of individual nuclei and the observable magnetization (and hence the detected signal) decays or "relaxes" exponentially (Fig. 7.2) with a time constant T_2.

$$M_{xy}(t) = M_{xy}(0)\exp(-t / T_2) \tag{7.5}$$

As the strength of the detected MRI signal is dependent on the total macroscopic magnetization precessing within the x–y plane, the detected signal also decays with the same time constant.

2.2.2 Longitudinal, T_1 or Spin–Lattice Relaxation

The second relaxation process (termed longitudinal relaxation) determines the rate at which the nuclei return to their equilibrium longitudinal polarization aligned back along the z axis with the main static field. During longitudinal relaxation, energy is

lost from the nuclei to the tissue with a second exponential time constant T_1 (Fig. 7.2e). If the applied RF pulse is calibrated to impart a 90° flip angle the recovery of the magnetization to equilibrium is described by:

$$M_z(t) = M_z(0)\{1 - \exp(-t/T_1)\} \tag{7.6}$$

The T_1 relaxation process is always slower than the T_2 decay of transverse magnetization, and in vivo, the observable signal disappears some time before the nuclei have returned to their equilibrium polarization (Fig. 7.2d, e). The processes driving relaxation at the tissue level are determined by the precise environment experienced by each proton. Differing tissue compartments therefore have different relaxation times which can be exploited to generate contrast in MRI images [2].

2.3 Localizing the Origin of the NMR Signal: MRI

In 1973 Paul Lauterbur published pioneering data demonstrating the potential for using the nuclear magnetic resonance phenomenon to generate images [3] and for which he shared the 2004 Nobel Prize for Medicine and Physiology with Peter Mansfield. MRI is based around a simple extension to Eq. (7.3). If a linear magnetic field gradient (G_r) is superimposed on the main static field B_o, the frequency of the resonant condition becomes dependent on the location in space, i.e.

$$\omega(r) = \gamma(B_o + G_r r) \tag{7.7}$$

as illustrated in Fig. 7.3. By applying the field gradient simultaneously with the applied RF pulse Eq. (7.7) indicates that the pulse will only (selectively) excite a signal from the region of sample with resonant frequency matching the bandwidth properties of the applied pulse. Alternatively by applying a field gradient during the time when the signal is being sampled a distribution of frequencies will be present in proportion to the distribution of nuclei in space, which can be determined by the mathematical construct of the Fourier transformation [4].

2.4 The Basic Elements of MRI Instrumentation

From the above description it is possible to identify the main components of the MRI instrumentation, these being

1. a uniform static magnetic field,
2. a RF system arranged to efficiently irradiate the sample with radio-waves,
3. a system to transiently impose a linear field gradient to localize the MRI signal,
4. a RF system to detect, demodulate and sample the excited MRI signal, and
5. a reconstruction and display system.
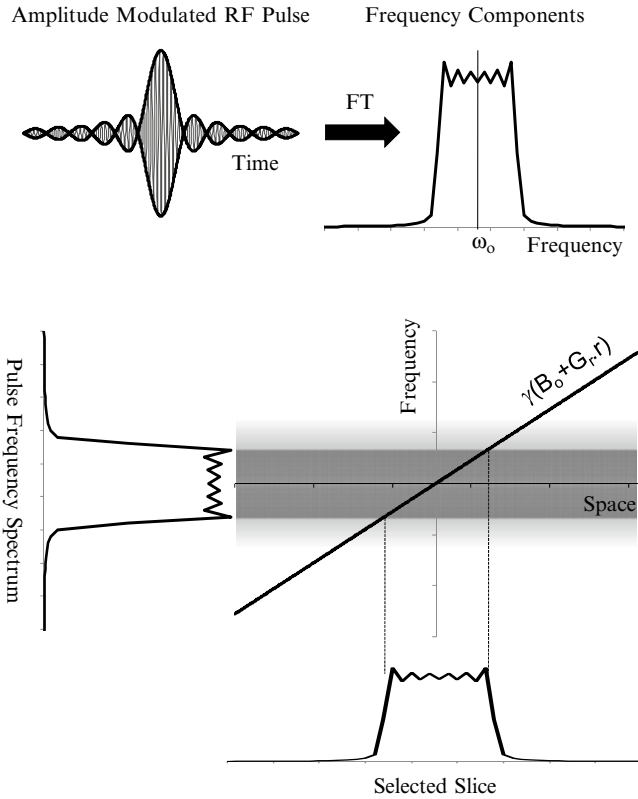
Fig. 7.3 The relationship between gradient field strength, MRI resonant frequency and the principle of slice selection. An amplitude modulated pulse of RF waves at the Larmor frequency (ω_o) has an effective set of frequency components given by the Fourier transform (FT). When applied in the presence of a field gradient G_r, the frequency spectrum of the pulse matches the resonant condition for only a small section of the object, exciting a signal from a selected slice

3 The MRI Scanner

A schematic diagram of the entire MRI instrument is shown in Fig. 7.4. In this section we consider the design criteria and selection of each of these components.

3.1 *Magnet*

The largest single component of the MRI scanner is the magnet system which generates the applied field B_o. Magnet design must be such that the field is highly uniform (homogeneous) and temporally extremely stable. It is convenient to describe these design specifications by considering the spatial frequency variation and
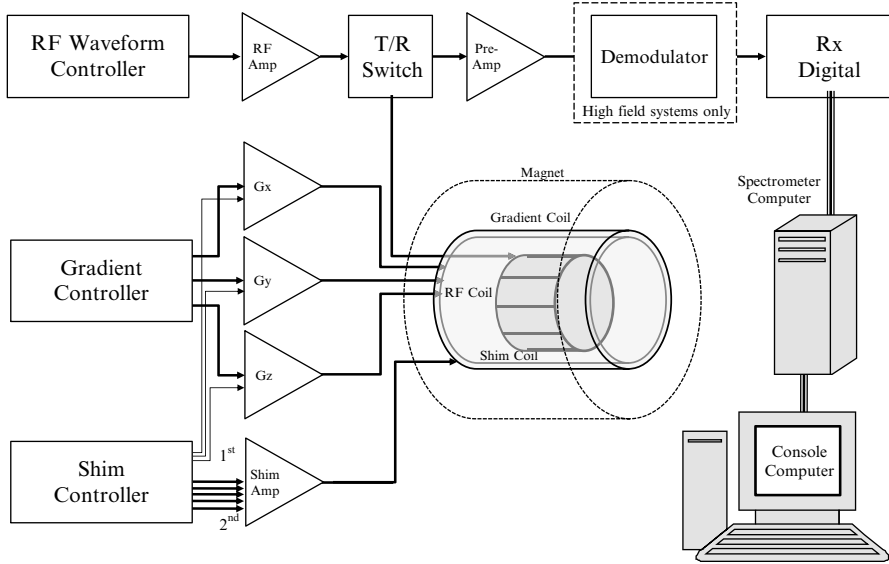
Fig. 7.4 Schematic diagram of the MRI scanner instrumentation

frequency stability they impart to an extended sample placed within the MRI scanner. Typically basic magnet homogeneity must be better than 0.1 parts per million (ppm) and stability must be of the order of a few Hz per hour (equating to a field drift of 1 part in 10^8 or better).

Examples of typical commercially available small-animal magnets are shown in Fig. 7.5, together with schematic illustrations of the internal design in Fig. 7.6. The majority of magnets for in vivo imaging are based around a similar design using a cryogenically cooled, superconducting, solenoid-type coil to provide a powerful and stable magnetic field. The solenoid itself is generally constructed from a niobium/titanium or niobium/tin alloy which becomes superconducting (the wire resistance is zero) below a critical temperature (T_c, 10 K for Nb/Ti, 18 K for Nb/Sn). The solenoid is suspended in a bath of liquid helium (boiling point 4.2 K). Once the main current has been established the ends of the solenoid can be joined via a superconducting switch to form a continuous loop, and the power-supply can be removed. The homogeneity of the magnetic field can be adjusted by passing current through additional field profile coils (the cryoshim coils) within the cryostat until the measured field is as uniform as possible. Slight residual resistance causes the field to decay with time, but this downward field drift is less than 1 part in 10^8 per hour. To maintain the superconducting state the solenoid is carefully thermally isolated from the rest of the magnet structure to minimize helium boil-off. Thermal isolation is enhanced by vacuum vessels and heat-shields. In traditional magnet designs a liquid nitrogen (boiling point, 77 K) vessel is also used (Fig. 7.6, lower left) as an additional heat shield for the helium bath. Boil-off of the relatively inexpensive liquid nitrogen is sacrificed in a bid to minimize helium boil-off. In this design, both

Fig. 7.5 Typical commercially available small animal MRI magnet systems. *Left*: A cryogenic unshielded ultra-high field 16.4 T small animal MRI magnet. For scale, the free bore diameter is 260 mm (courtesy of Varian Inc). *Right*: A 7 T, 300 mm bore ultra-shielded magnet with pulse-tube cryocooler for minimal helium boil-off (courtesy of Bruker Biospin Ltd)

cryostats must be refilled with cryogens on a frequent basis (weeks to months). More recent magnet designs incorporate a refrigeration system (the "cold head" and associated components, based on the pulse-tube refrigeration method of Gifford and Longsworth [5]) to re-liquify helium vapor within the magnet, minimizing boil-off (Fig. 7.6, lower right) and reducing cryogen costs, but at the expense of refrigeration costs. All magnet systems must be connected to a *quench pipe* to allow safe release of cryogen gas in the event of magnet failure when rapid and uncontrolled boil-off of cryogens can occur.

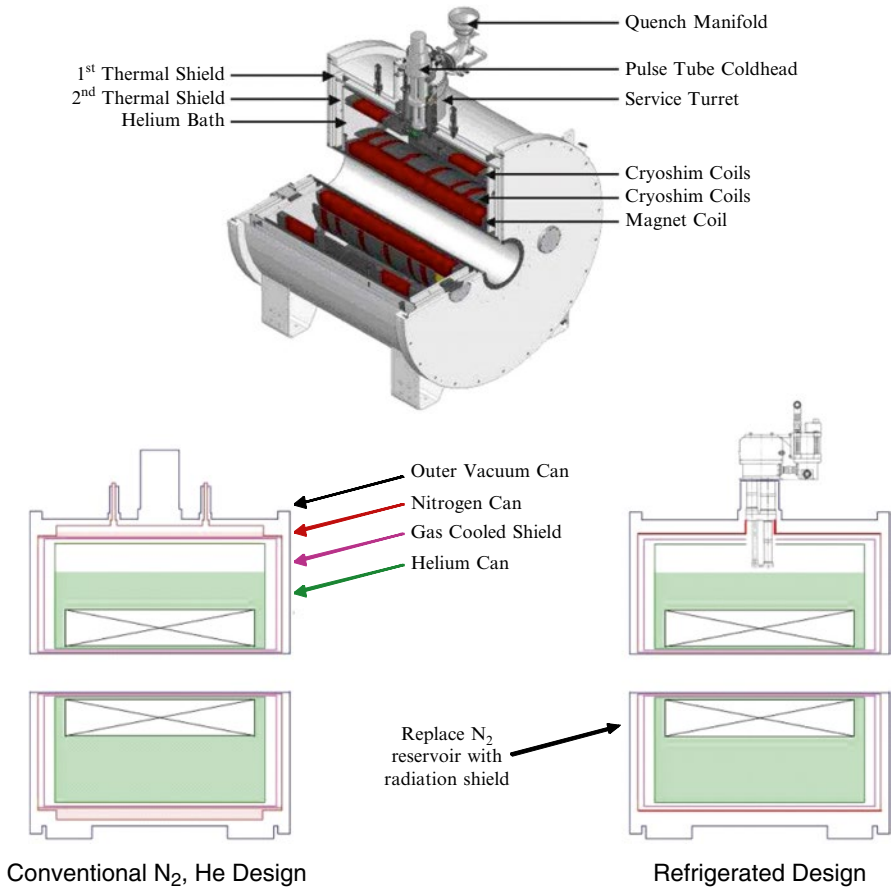### 3.1.1   Selection of Magnetic Field Strength

In Sect. 2.1 we described that the proton nucleus has two energy levels in the applied magnetic field. From a macroscopic perspective the many nuclei within a sample are distributed between these two levels and, on average, the difference in the number of nuclei (Δn) which populate each of these energy levels can be described by

$$\Delta n = n_{\alpha} - n_{\beta} = N\Delta E\,/\,2KT \tag{7.8}$$

where N is the total number of nuclei, n_{α} and n_{β} are the number of nuclei in each of the two levels, K is the Boltzmann constant and T is the sample temperature. Equation (7.8) shows that this distribution is driven by the thermal energy of the nuclei. Combining Eqs. (7.1) and (7.8) we find that the fractional difference in occupancy of the energy levels is

$$\frac{\Delta n}{N} = \frac{\gamma h B_o}{4\pi KT} \tag{7.9}$$

1st Thermal Shield
2nd Thermal Shield
Helium Bath

Quench Manifold
Pulse Tube Coldhead
Service Turret

Cryoshim Coils
Cryoshim Coils
Magnet Coil

Outer Vacuum Can
Nitrogen Can
Gas Cooled Shield
Helium Can

Replace N_2
reservoir with
radiation shield

Conventional N_2, He Design

Refrigerated Design

Fig. 7.6 Schematic diagrams of the internal structure of the cryogenic and cryocooled magnet systems. The main magnetic field is produced by the *Magnet Coil* with additional field from the *Cryoshim Coils* which are adjusted to obtain the optimum magnetic field uniformity. *Left*: A cryogenic magnet design where liquid nitrogen and helium boil-off requires regular re-filling of the magnet dewars to maintain superconductivity. *Right*: A cryocooled magnet design where the nitrogen vessel is no longer necessary and helium vapor is recondensed back into the dewar leading to minimal boil-off in normal operation. The heat exchanger and chiller system required to cool the "cold head" are not shown in this illustration (courtesy of Varian Inc)

The observable signal strength depends directly on this excess difference in occupancy between the energy levels which at achievable field strengths of between 0.1 and 10.0 T is only 1 in 2,870,000–28,700 nuclei. Thus the basic nuclear magnetic resonance phenomenon is actually inherently insensitive.

From Eq. (7.9) it is clear that there are two options to obtain a stronger MRI signal; operate at the highest possible magnetic field strength B_o, or decrease the sample temperature. This second approach is not compatible with in vivo imaging where core body temperature must be maintained within physiological limits, which

Table 7.1 Typical field strengths used for in vivo MRI investigation together with proton frequency ($\gamma(^1H) = 4.25 \times 10^7$ Hz/T) and available bore sizes (maximum size of object)

Field strength (T)	Proton frequency (MHz)	Typical bore size (mm)	Purpose
1.5	63.75	600	Clinical imaging
3.0	127.5	600	Human/pre-clinical imaging
4.7	200.0	160–400	Human/pre-clinical imaging
7.0	300.0	160–400	Human/pre-clinical imaging
9.4	400.0	160–400	Human/pre-clinical imaging
11.7	500.0	160–400	Pre-clinical imaging

leaves field strength as the only viable option. We will discuss advanced methods to generate hyperpolarization in Sect. 4.2. Therefore in general, higher field strength equates with increased signal to noise ratio in the MRI image and the highest possible field strength (within economic limits) is strived for. Table 7.1 lists typical field strengths used for in vivo imaging and the respective proton frequencies.

3.1.2 Siting-Shielding, Filtering, Fringe Field

Since the signal detection system is a high sensitivity RF receiver, shielding from stray RF signal sources in the local environment is critical for obtaining maximum sensitivity and eliminating image artifacts. Radio-frequency signals can penetrate down the scanner bore where they are detected by the system RF coil and enter the scanner via the signal pathway. The degree of penetration of RF noise along the bore depends on the dimensions (bore radius to magnet length ratio) with the bore itself acting as a waveguide providing some signal attenuation. To eliminate all extraneous noise sources the magnet is normally sited within, and earthed to a Faraday cage. All electrical connections to and from the magnet (e.g. scanner hardware connections, or user equipment such as animal monitoring) pass through electronic filters in the Faraday cage wall to remove signal within any of the required operating frequency ranges of the system. An alternative to a full Faraday cage is to electrically "seal" the ends of the magnet bore with metal plates once the sample is positioned with the magnet, essentially creating a Faraday cage from the scanner bore and the end plates (Fig. 7.7).

The polarizing field present at the magnet isocentre is many thousands of times the earth's field (the earth's field is typically 0.05 mT) and decays with distance from the magnet structure. This *fringe field* extends into the scanner laboratory and poses several hazards to MRI scientists and must be carefully controlled [6], (Fig. 7.8). The largest hazard is to staff with active implanted medical devices such as cardiac pacemakers. These devices can be activated or damaged by interaction with the magnet fringe field, with potentially life threatening consequences. A safe working zone outside the 0.5 mT fringe field line must be established and inside which persons with such devices must not be allowed. Careful screening of staff can

Fig. 7.7 Illustration showing a magnet with integral Faraday cage (courtesy of Bruker Biospin Ltd)
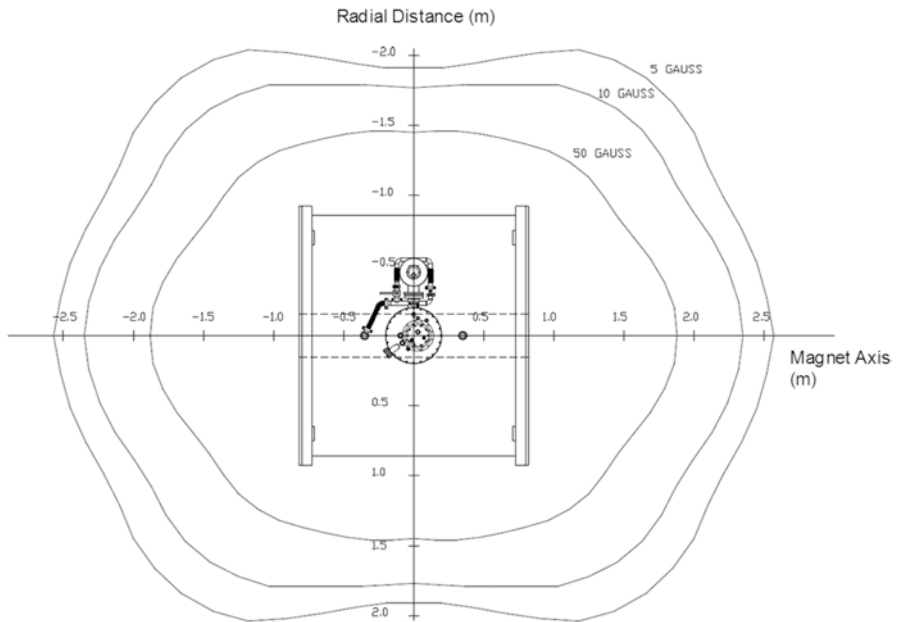

Fig. 7.8 Fringe field plot for a typical self-shielded small animal MRI scanner with 210 mm bore operating at 9.4 T (courtesy of Varian Inc)

eliminate risk. The fringe field however also exerts an attractive force on any ferromagnetic items in the vicinity. Loose metal objects can be attracted to the scanner with such force that they become projectiles, injuring staff and causing major damage to the magnet structure. Again, careful design and monitoring of the scanner environment is crucial and can minimize this risk. Typically the requirements for a Faraday cage and safe working zone can be combined such that the 0.5 mT line is contained entirely within the Faraday cage.

Current magnet systems for small animal studies incorporate a self-shielding magnet design, whereby a second set of coil windings are positioned within the magnet cryostat. These are counter-wound to the main coils with a density of turns such that the fringe field from the primary windings is partially counteracted by the field from these screening windings. This design creates a compact installation footprint for the system. As an alternative to active self-shielding passive shielding can be incorporated by designing a steel enclosure around the magnet which contain the magnetic field.

3.2   Gradient System

In Sect. 2.3, we described how the localization of the MRI signal is performed using time-varying linear field gradients which are modulated during the MRI sequence. These fields are created by the system gradient coils. The desired gradient waveform is generated by the spectrometer gradient waveform control processor and fed to the gradient coils via high power linear constant current gradient amplifiers.

3.2.1   Gradient Coils

In order to localize the MRI signal in three dimensions the scanner is equipped with three orthogonal and independent gradient coils constructed around a series of concentric cylindrical formers. These are largely based on a Maxwell coil design for the z gradient and Golay coil designs [7] for the x and y gradients as illustrated in Fig. 7.9. As with the magnet structure, the magnetic field created by current flowing in the gradient coils is not confined to the gradient tube bore but has a fringe field component which extends around the coil structure. Rapid switching of the field gradients can induce eddy currents to flow within any conducting surface in the vicinity, particularly in components of the magnet cryostat. These eddy currents generate their own time-varying magnetic field which distorts the field generated by the gradient coil itself, leading to image artifacts and instabilities. The time constant of these eddy-currents is inversely proportional to the resistance of the conductors in which they flow, so it is imperative that no eddy currents are allowed to form in the cooled internal structures of the magnet system, where time constants can be several seconds. To counteract this problem, Mansfield introduced the concept of actively shielded gradient coils [8] which again contain a second counter-wound set
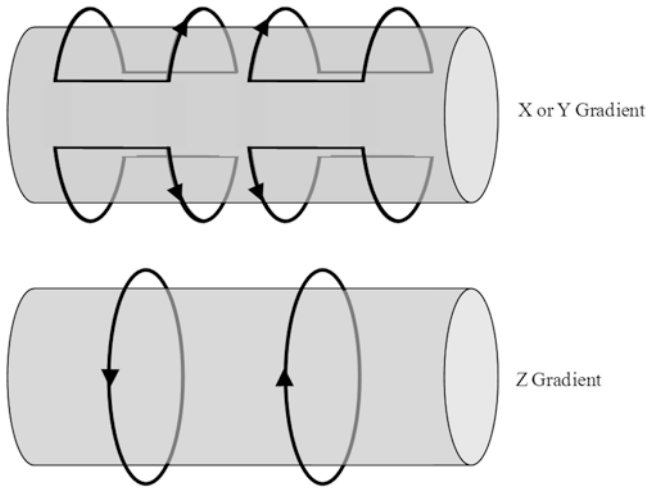
Fig. 7.9 Schematic diagram of the current windings for the three axes of the gradient coil. Over the useable volume of the scanner the windings all produce linear variations in the Z magnetic field (i.e. $\partial B_z/\partial x$, $\partial B_z/\partial y$ and $\partial B_z/\partial z$ the z axis being defined along the magnet bore)

of windings on a co-axial former surrounding the main gradient coils. Typically active shielding of the gradient coils reduces eddy currents to below 1 % of the equivalent unshielded design. A commercial gradient system (un-mounted from the magnet) is shown in Fig. 7.10.

Image resolution Δr is determined by the maximum gradient strength which can be established across the sample during detection of the MRI signal. The precise relationship is defined by the expression

$$\Delta r = \frac{2\pi}{\int_0^t \gamma . G_r\left(t'\right) . dt'} \qquad (7.10)$$

where $G_r(t')$ is the time-varying field applied over duration t for which the MRI signal is sampled.

Gradient strength is determined by the coil geometry and the current (I) passing through the windings. Gradient strength is inversely proportional to the coil radius so choice of the optimum gradient coil is dictated by the largest sample size which is to be imaged. The rate at which each gradient field can be switched to encode spatial information during the imaging sequence is determined by the self-inductance (L) of the coil, the applied voltage (V) and the total resistance of the system (R, from the coils and cabling). This can be expressed as

$$V = IR + L\frac{dI}{dt} \qquad (7.11)$$
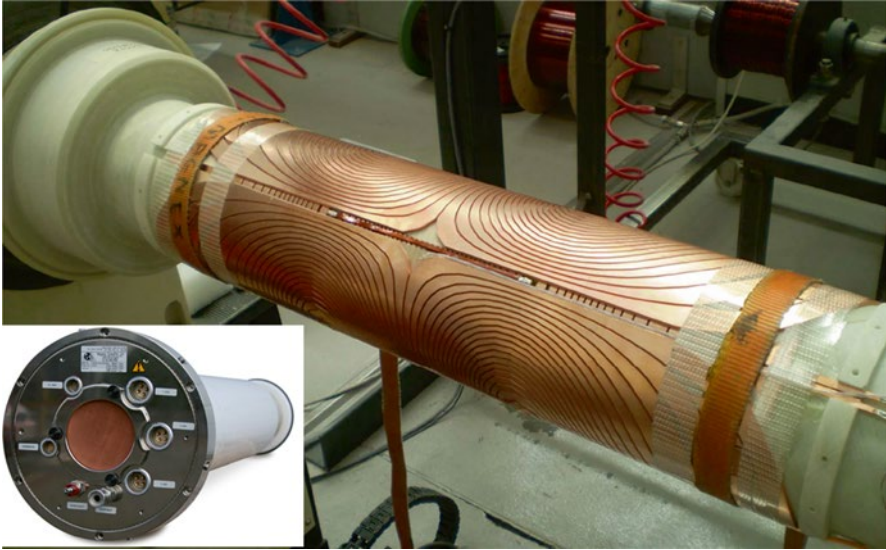
Fig. 7.10 View of a gradient coil during construction. The current paths illustrated in Fig. 7.9 are translated into patterns of continues arcs of copper cut from a single sheet. Sheets for each of the primary and secondary (shielding) windings are positioned around a glass reinforced plastic former interspersed with insulation. Shown is one of the transverse windings (X or Y), with another winding visible below. The whole structure is finally embedded in epoxy resin under pressure. *Inset*: View of the complete gradient coil showing connections for the three gradient coils, integrated shim coils, thermometry and water cooling (courtesy of Varian Inc)

Rapid gradient response (dI/dt) is essential for modern ultra-rapid imaging sequences and gradient coils are therefore designed to have low self-inductance and resistance and are driven at high current and high voltage. Small animal systems typically are driven with amplifiers supplying peak voltage of 300 V and peak current of 200 A generating gradient fields between 400 and 1,000 mT/m depending on gradient coil diameter.

The final element of the gradient hardware is the cooling system. High duty cycle scanning leads to intense heat dissipation in the gradient coils. In the context of the imaging experiment this heating can alter the coil resistance changing the coil performance, while in the context of the coil hardware the heating can cause damage to the coil windings. Water cooling systems are therefore incorporated within the coil structure in close thermal contact with the coil windings and supplied with chilled water to maintain a constant working temperature.

3.2.2 Pre-emphasis

In Sect. 3.2.1 the concept of active gradient shielding was introduced as a method to reduce eddy current interactions with the magnet structure. While good gradient design is effective in eliminating ~99 % of the stray field effects, residual eddy
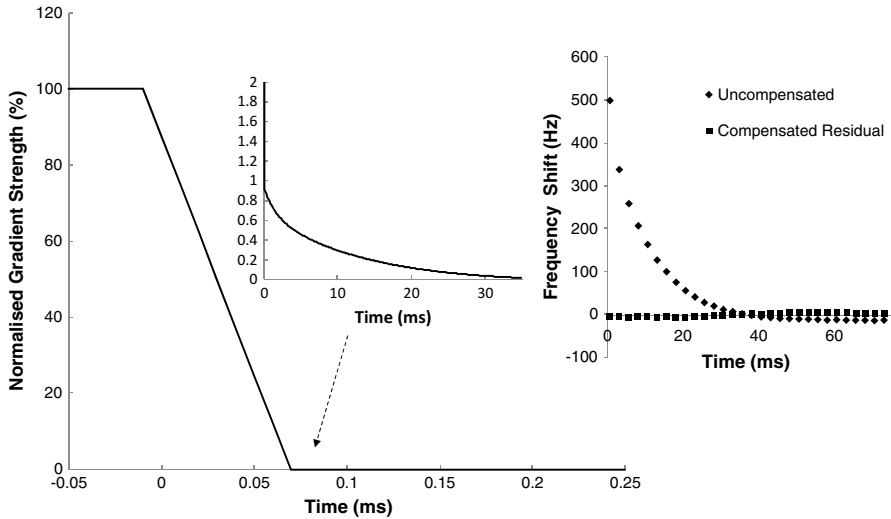
Fig. 7.11 Illustration showing the falling edge of a requested trapezoidal gradient waveform. Experimental measurement of field stability in the scanner bore following the gradient waveform showed time-varying eddy-current gradient fields within the magnet bore with three different time constants of 1.5, 13.5 and 65.5 ms. Pre-emphasis adjustment to provide a stable measured field required addition of time-decaying components with these time constants at −0.09, 0.75 and 0.24 % of the requested gradient amplitude and leads to a gradient function which has a long tail (insert, note the much longer time scale). Also shown is the measured frequency shift in a small object in the scanner as a function of time after the end of the ideal gradient event, with and without pre-emphasis compensation

currents are still present in the system. Gradient field strengths of 100 mT/m are not uncommon in small-animal scanners which amounts to a proton frequency dispersion [Eq. (7.7)] of 425,000 Hz/cm. The frequency stability of the scanner is measurable within the receiver electronics (see Sect. 3.4.3) to typically better than 0.1 Hz and several data acquisition methods (notably MRI spectroscopy acquisitions and the echo-planar imaging or EPI sequence) are sensitive to field changes of ~0.1–5 Hz. Therefore residual eddy currents of 1 % are still intolerable for high sensitivity imaging. The residual field can however be reduced significantly using the technique of *pre-emphasis*.

Pre-emphasis refers to the adaptation of the driving waveform such that the magnetic field gradient produced by the coil combined with the field produced by the induced eddy currents produce the true desired gradient field modulation within the sample (Fig. 7.11). Pre-emphasis is a function of the interaction between the individual system components (magnet, gradient coil and RF coil) and is pre-measured for each configuration during system installation. The time-varying eddy currents are mapped for each gradient axis and decomposed into a series of exponentially decaying functions and amplitudes. From these parameters the gradient driving function is "pre-emphasized" before passing to the gradient coils.

3.3 Shims

In Sect. 3.1 we noted that the applied magnetic field B_o must be highly homogeneous so that the Larmor frequency is as close to uniform as possible. However, even if a *perfect* magnet design could be constructed this would not achieve optimal conditions. Differences in the magnetic susceptibility (χ) between air and the object to be scanned lead to spatial variations in the magnetic field established within the sample, and hence to local variations in B_o. As static field strength is increased the magnitude of the inhomogeneity variation increases, while the size of the object typically decreases (higher field systems generally have smaller bore size, Table 7.1) and the relative proportion of the object experiencing unacceptable field variation increases. This field distortion must be therefore compensated in each object which is scanned via a process known as magnetic field *shimming*.

Within the magnet bore an additional set of field profile coils (the *shim coils*) are added. The winding geometry of these coils is designed to create static fields with first, second and in some cases third order spatial spherical harmonic distributions [7, 9]. The spatial field variation can be mapped using specific data acquisition sequences (e.g. [10]), decomposed into their spatial harmonics and then corrected by driving appropriate current into each shim coil. In general shim fields are static fields, but in some conditions dynamic shimming to alter the field shim on a per collection basis can improve sensitivity [11, 12]. Shim coils can be mounted separately within the magnet bore, but in most system designs they are incorporated within the gradient coils located in the space between the primary and secondary (screening windings), thus saving valuable free bore space.

3.4 RF System

The second major system within the MRI instrument is the radio-frequency (RF) chain, consisting of components to transmit the initial excitation pulse and subsequently detect and demodulate the returning MRI signal.

3.4.1 RF Coils

The radio-frequency coil is required to transmit the excitation pulse into the sample. The coil is in essence a RF antenna which has been specifically designed to deposit RF energy within a confined volume (rather than to radiate energy away from the coil as in a RF aerial). RF coil systems fall into two basic categories, (1) single transmit-receive coils and (2) separate transmit and receive coil pairs. In either case, the basic coil design consists of a tuned circuit (inductance and capacitance networks with the main inductance formed from the coil winding) which resonates at the Larmor frequency of the nucleus of interest. It is well recognized in electronic theory that resonant circuits provide a scaling of the current flowing within the circuit by the quality
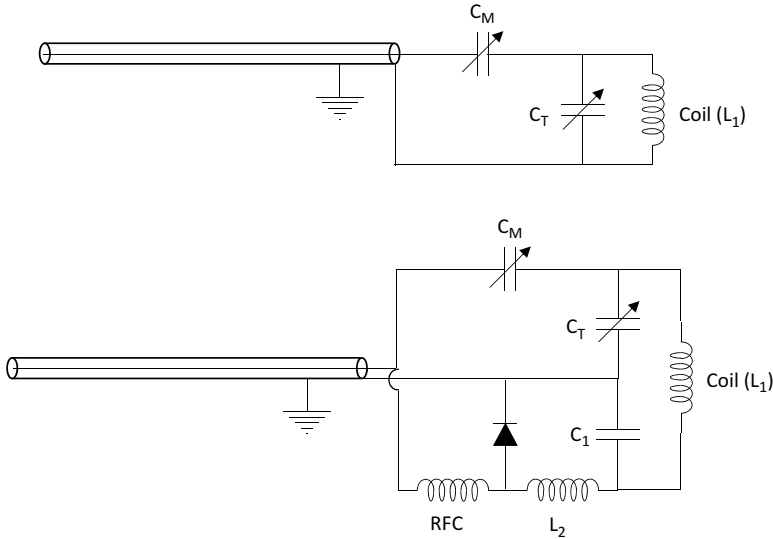
Fig. 7.12 Basic circuit diagrams for RF coil designs. The coil conductors which produces the RF field form the main inductance (L1) of the system while additional tuning (CT) and matching capacitors (CM) complete the resonant circuit and allow the coil to be tuned to the appropriate scanner frequency and matched to 50 W impedance for optimum power transfer between the coil and rest of the system electronics. A more advanced coil design (*lower*) is also illustrated which could be used as a receive only coil within a larger volume transmit coil. Additional components in this design allow the coil to be detuned from the Larmor frequency via PIN diode switching. During RF excitation by a second coil a DC bias is supplied to the PIN diode via the RF choke (RFC) placing the additional inductance L2 in parallel with tuning capacitor C1 leading to an altered resonant frequency. During signal reception the PIN diode is off and inductance L2 no longer contributes to the coil resonant frequency

factor Q of the coil (Q being the ratio of the resonant frequency to the half width of the resonance), providing increased performance when working at that resonant frequency relative to an untuned circuit. Simple circuit diagrams showing the essential elements of the RF coil are shown in Fig. 7.12. As the electronics of the RF chain are designed to operate at 50 Ω impedance (resistive) the RF coil must also be matched to 50 Ω to maximize power transfer between the components of the RF chain.

Current flowing within the windings or conductors forming the coil generates a magnetic field oscillating at the driving (Larmor) frequency and it is the magnetic component of this near field (denoted B_1) which interacts with the nuclei in the imaging experiment.

When a simple imaging experiment such as a "spoiled gradient recalled imaging" [13] (SPGR) measurement is performed in a sample with relaxation times T_1 and using a sequence with repetition time TR, the strength of the excited MRI signal, $S(r)$ arising from a location r is described by the expression

$$S(r) \propto \rho(r) \frac{\left(1 - e^{-TR/T_1}\right)\sin\alpha}{1 - \cos\alpha . e^{-TR/T_1}} \qquad (7.12)$$
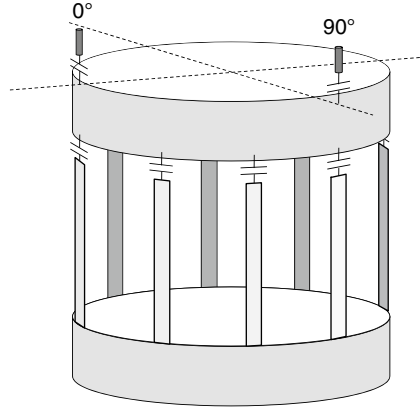
Fig. 7.13 Schematic diagram of the birdcage volume coil design. The coil is tuned to the Larmor frequency by adjusting the capacitance at each "rung". Although this structure will resonate at a number of frequencies, the required mode occurs when a RF standing-wave of wavelength equal to the circumference of the end rings propogates within the structure. In this case current flow down each rung is distributed sinusoidally around the coil leading to a uniform magnetic field distribution within the active volume of the coil

where $\rho(r)$ is the density of nuclei at location r and α is the flip angle produced by the RF pulse [Eq. (7.4)]. Flip angle α is determined by the RF pulse duration tp and the local B_1 field strength which can vary with position r depending on the design of the RF coil (see below) leading to the expression

$$\alpha(r) = \int_o^{tp} \gamma B_1(r,t')\,dt' \tag{7.13}$$

Further, via a principle known as *reciprocity* [14], the sensitivity of the RF coil used in signal detection is proportional to the effective $B_1(r)$ distribution of that coil. From these two expressions it is clear the careful control of the B_1 field distribution within the sample is essential.

In general the larger the RF coil, the lower the inherent sensitivity. (This follows from reciprocity since the magnetic field generated by unit current flowing in a larger coil structure will be less than the same current flowing in a smaller structure). Close coupling of the smallest coil system with the object being imaged provides maximal signal to noise ratio. It follows that for optimum sensitivity RF coil design must be tailored to the investigation or object being scanned.

Typically for body imaging a surrounding "volume" coil is used which may be used to both transmit and receive the MRI signals, or may be used in transmit only mode with a local receiver coil positioned over the target region to obtain greater sensitivity. A simple volume coil based on the birdcage design [15] is illustrated in Fig. 7.13. The birdcage design was the first MRI coil to have essentially uniform B_1 field distribution. Through appropriate distribution of capacitance around the rungs
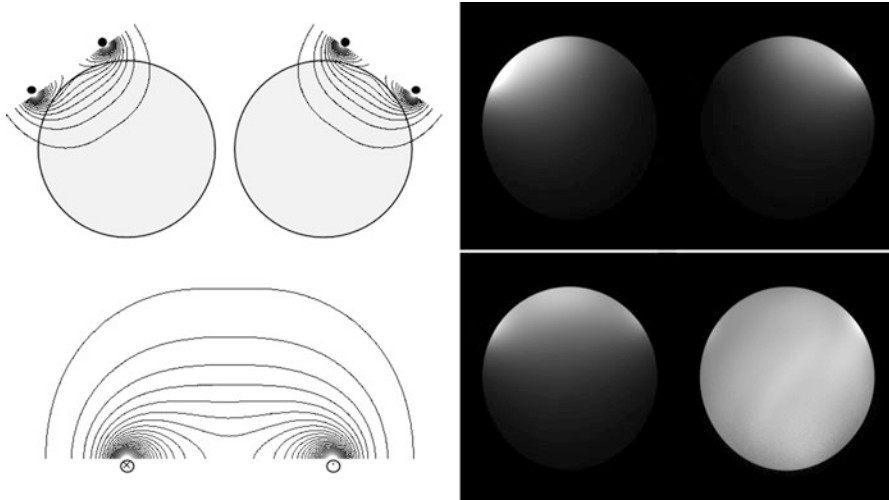
Fig. 7.14 Theoretical and experimental images showing the received signal from individual coil elements of a phased array coil and the image created by mathematical combination of the signal from the individual elements. *Lower left*: Theoretical B_1 field variation with distance from the plane of a single circular loop surface coil. *Upper left*: Contour plots of the theoretical B_1 profiles for a phased array surface coil pair overlaid on schematic of a test object. *Upper right*: Experimental data showing individual images reconstructed from signals received through each independent receiver coil. *Lower right*: Quadrature combination of the signals from the two coils (*left*) and SENSE reconstruction of the signals using a sensitivity reference scan (*right*)

or end-rings of the structure current flow down each rung is arranged to be sinusoidal in amplitude when driven at the resonant frequency, leading to constructive interference of the field from each rung and generating the uniform B_1 distribution. When driven from a single location on the end-ring (linear drive), current flow around the structure can be in either direction, generating two counter rotating B_1 fields, only one of which couples to the sample nuclei. However, by driving the coil from two locations 90° apart and with signal phase also separated by 90° (in *quadrature*, Fig. 7.13) a single rotating field is produced, providing a factor of 2 in power performance for RF pulse transmission. In receive mode, the precessing magnetization inductively couples to the coil structure and in the case of the quadrature design is coherently detected through both channels. Although the signal source is coherent, noise is incoherent and quadrature combination of the two channels leads to a $\sqrt{2}$ improvement in signal to noise ratio compared to linear mode reception.

Surface coils and phased array coils. When the volume to be imaged is superficial and is limited in lateral extent (for example if investigating a subcutaneous tumor where the precise location is known, or for brain imaging investigations) then alternative coils termed *surface coils* can be employed to give high sensitivity images. A surface coil consists of an approximately planar coil configuration which is positioned adjacent to the area of interest [16]. The theoretical B_1 field distribution [17] for one such a coil consisting of a single circular loop is illustrated in Fig. 7.14. It can be seen that the strongest B_1 field is produced close to the loop and falls away
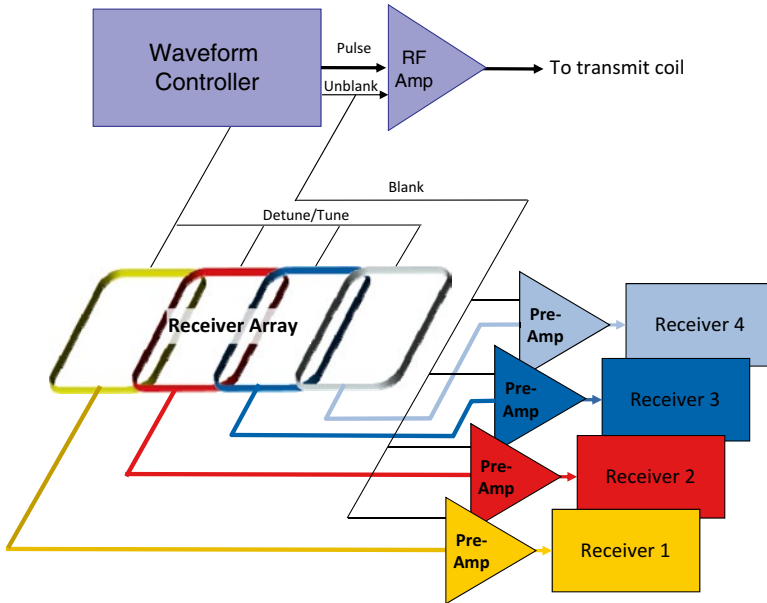
Fig. 7.15 Schematic diagram of a phased array coil system

rapidly with distance from the coil. By reciprocity the imaging sensitivity is also maximal close to the coil. Surface coils can also be designed to work as quadrature systems using two uncoupled, angled and overlapping coils. Although true quadrature coils require perfectly orthogonal B_1 fields, which can never be produced from the field distribution from a planar structure, a focused area of the B_1 field from the quadrature surface coil does meet this criteria and signal from that region of the sample does benefit from quadrature signal to noise ratio (SNR) improvement.

The concept of surface coils was developed further for clinical MRI applications by the introduction of phased-array RF coils by Roemer in 1990 [18]. This coil design uses an array of overlapping but electrically uncoupled surface coils each connected to its own complete receiver channel (Fig. 7.15). Individually each coil element provides the high sensitivity expected from the small loop coil with the associated limited field of view, but the data from the whole array can be combined to provide a much greater total imaging field of view (Fig. 7.14). Volume coils can be also constructed using similar principles by positioning the array of smaller coil elements around a cylindrical former. Multi-element array coils are most often used as "receive only" coils in conjunction with a separate surround volume coil which provides uniform RF excitation. In this configuration the transmit and receive coils must be electrically uncoupled for maximum performance and most importantly to prevent the high power excitation pulse from entering the high sensitivity RF receiver chain. Coil system are therefore actively uncoupled using PIN diode switches to tune or detune each coil [19], (Fig. 7.12).
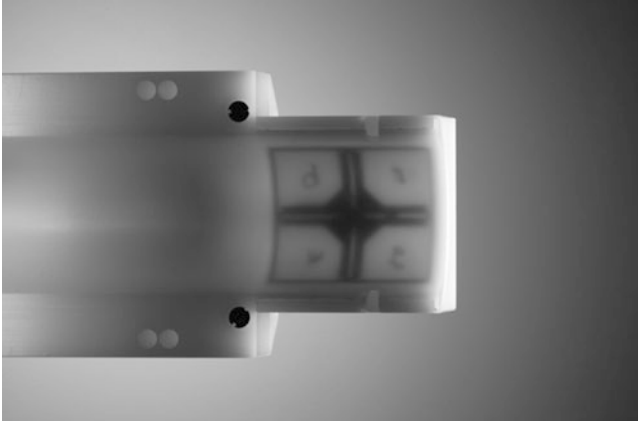
Fig. 7.16 Commercially available surface coil array for neuroimaging. The internal coil elements can be seen through the housing (courtesy of Bruker Biospin Ltd)

The engineering challenge in constructing separate transmit and multi-element receive array coils structures at small scale into devices for small animal MRI has recently been addressed (Fig. 7.16).

Cryocooled Coils. The sensitivity of the scanner hardware can be quantified in term of the signal to noise ratio of the acquired images. As we have discussed above, the signal strength depends on many factors including static field strength, the amount of magnetization within the active volume of the RF coil, the RF coil size and geometry. Likewise, noise within the image dataset (the random fluctuations seen on top of the image) has several potential source; noise arising within the object being scanned and coupled into the RF coil, electronic noise generated within the RF coil itself, and electronic noise generated downstream of the RF coil in the receiver electronics (see below). In a well designed system this latter source is small. The source of electronic or "*Johnson*", "*Nyquist*" or simply "*thermal*" noise is attributed to the chaotic motion of electrons within any components giving resistance to the circuit. This thermal noise N can be expressed by

$$N \propto \sqrt{4KTR} \tag{7.14}$$

where R is the electronic resistance and T the temperature of the electronic circuitry or coil (K is the Boltzmann constant). Electronic noise originating in the RF coil components can therefore be reduced by cooling the coil structure. *Cryocooled coils* are common in chemistry applications of NMR and are becoming available for in vivo use based on both helium and nitrogen refrigeration systems (Fig. 7.17). Design of cryocooled coils for animal imaging requires careful insulation of the cold components from the animal which necessarily increases coil size and hence the separation between the coil and the animal. There is therefore a trade-off between lowering noise and lowering signal.
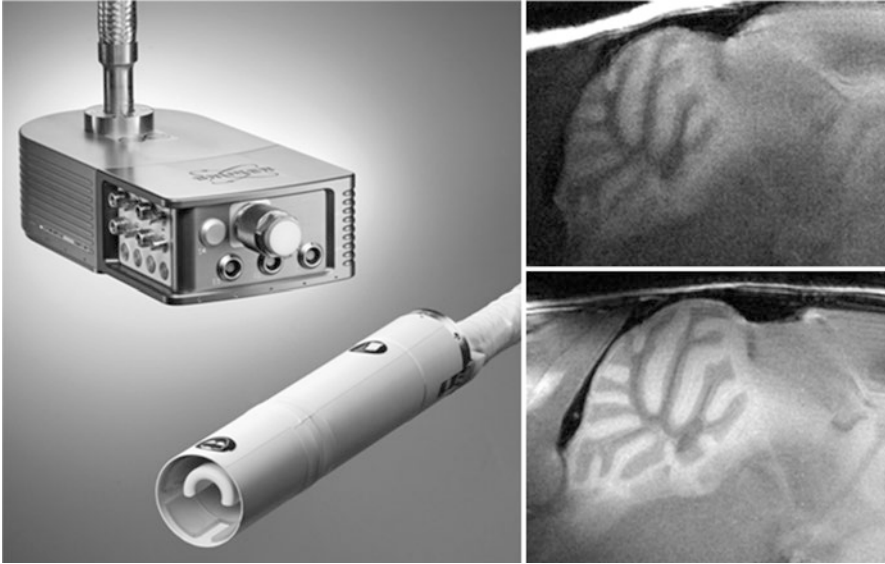
Fig. 7.17 Illustration showing a commercial cryo-cooled RF coil and illustrating the improvement in image quality which can be obtained by cooling the coil structure and associated pre-amplifier. Images were collected under identical conditions using a RARE sequence, eight echoes; TR/TE: 5,000/53 ms, 1 mm slice thickness and in-plane resolution of 40 μm×40 μm (courtesy of Bruker Biospin Ltd)

3.4.2 RF Generation System

The RF pulse applied to excite the MRI signal is generally a complex amplitude and phase modulated pulse whose characteristics determine the precise nature of the excitation such as the profile of the selected slice. The pulse waveform is generated by a dedicated processor board in the spectrometer console. The basic pulse frequency must match the Larmor condition for the imaging slice of interest [Eq. (7.7)]. This process is performed by direct digital synthesis of the amplitude modulated pulse which is then shifted in frequency to the desired carrier signal produced by a highly stable synthesizer (e.g. PTS, Fig. 7.18). The final pulse shape is then fed to a high power (typically ~1 kW) linear amplifier which drives the RF coil. Since the RF pulse is an intense burst of energy with peak powers of many hundreds of Watts, the receiver electronics is "blanked" to prevent penetration into the high gain pre-amplifiers used to detect the micro-milliWatt MRI signal returning from the sample.

3.4.3 Receiver System

The receiver system is illustrated schematically in Fig. 7.19. The system begins with the receiver RF coil collecting the MRI signal from the precessing magnetization. This is fed directly to a high gain, low noise pre-amplifier which is often integral to
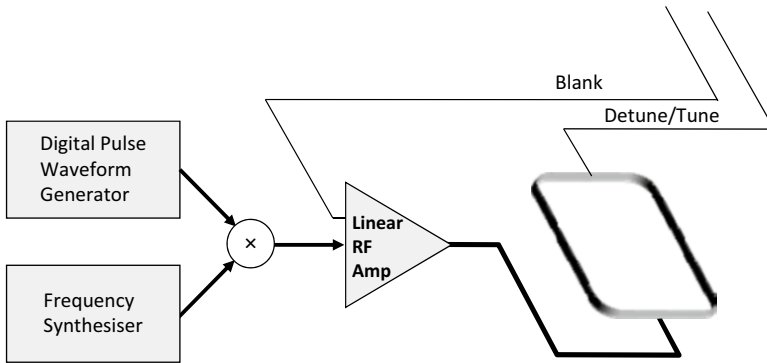
Fig. 7.18 Schematic of a typical RF transmission stage for a high field MRI scanner. The basic amplitude and phase characteristics of the required pulse are generated in digital form by the RF pulse waveform controller before being combined with a carrier signal at the required Larmor frequency

the RF coil. Amplification of the weak MRI signal at this earliest stage minimizes the potential for contamination by external noise sources. The RF signal is then demodulated down to the audio frequency range and split into a complex signal using a pair of phase sensitive detectors. Finally the two channels of the complex signal are digitized and stored in spectrometer memory before being saved to disk. Signals are filtered to eliminate noise from outside of the sampled signal bandwidth which may be performed using analogue filtering prior to sampling or digital filtering of the sampled signal.

3.4.4 Specific Absorption Rate

It is clear from the discussion above that significant amounts of RF energy may be applied to the sample, the majority of which will be absorbed by the tissue. This RF energy has the potential to raise tissue temperature which can lead to alterations in tissue physiology and in extreme cases RF burns. In clinical MRI scanners RF energy (or *specific absorption rate*, SAR) is closely monitored (both by calculation of the requested RF power and by experimental monitoring of RF output) and must remain below stringent legal requirements. SAR levels are defined in terms of local and global heating effects such that temperature rises of no more than 1 °C can be induced in patients [6]. Similar requirements are not so rigidly enforced in small animal MRI and many instruments do not contain the same RF monitoring circuitry found in their clinical counterparts. However, careful assessment of SAR is still essential as part of rigorous scientific practice.
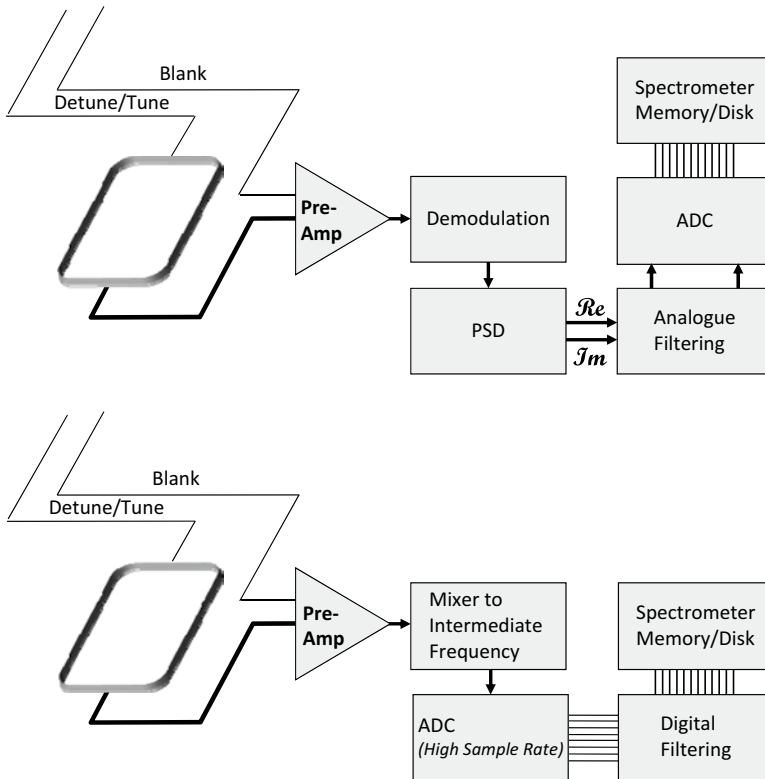
Fig. 7.19 Schematics of RF receiver systems for a high field MRI scanner. *Upper*: Traditional design based on analogue circuitry. The weak MRI signal is detected in the RF coil and immediately amplified using a low noise preamplifier circuit. The RF signal is then demodulated down to the audio frequency range and split into a complex signal using a pair of phase sensitive detectors. Signals are filtered to eliminate noise from outside of the desired signal bandwidth using analogue filtering prior to sampling. Finally the two channels of the complex signal are digitised and stored in spectrometer memory before being saved to disk. *Lower*: Digital design. The pre-amplified signal is mixed down to an intermediate frequency still in the 10 s of MHz range before being directly sampled at high bandwidth (e.g. 80 MHz). Digital filtering is applied to achieved the normal quadrature signal

3.5 *Data Reconstruction*

The sampled MRI data consists of time-varying signals whose frequency components are determined by the spatial water distribution and the applied spatial encoding gradient [Eq. (7.7)]. The generalized expression describing the MRI signal is given by

$$S(t) = \oint M_{xy}(r) \exp(-t/T_2) \exp\left(-i\left[\omega_o + \int_0^t \gamma G_r(t') r\, dt'\right]\right) dr \qquad (7.15)$$

Ignoring relaxation and demodulating the signal from the basic Larmor frequency simplifies this expression to

$$S(t) = \oint M_{xy}(r) \exp\left(-i\int_0^t \gamma G_r(t') r \, dt'\right) dr \qquad (7.16)$$

The gradient-time integral can be combined [20, 21] to introduce the term

$$k_r = \int_0^t \gamma G_r(t') \, dt' \qquad (7.17)$$

to describe the effect of gradient modulation, which further simplifies Eq. (7.16) to

$$S(t) = \oint M_{xy}(r) \exp\left(-ik_r . r\right) dr \qquad (7.18)$$

indicating that the time varying signal is simply the Fourier transformation of the spatial magnetization distribution measured along the direction of the applied magnetic field gradient G_r. Recovering the image is a simple matter of Fourier transformation (in one, two or three dimensions depending on the nature of the imaging sequence used).

Modern PCs have sufficiently fast processing speed that fast Fourier transformation can be performed by the console computer without the need for dedicated processing systems.

4 Advanced MRI Methods and Instrumentation for Molecular Imaging

So far we have described the generic instrumentation for MRI which measures the abundant proton signal from water molecules. While the anatomical images created by conventional MRI provide useful detail on tissue structure they do not achieve the goal of molecular imaging to provide information on the distribution of cellular and metabolic processes in vivo. With additional advanced instrumentation and the use of nuclei other than the proton, magnetic resonance can also contribute directly to molecular imaging.

4.1 Non-proton Techniques

Many (but not all) nuclei exhibit the phenomenon of nuclear magnetic resonance and can in theory be used in molecular or metabolic imaging studies. Key nuclei which have been used in biological investigations are given in Table 7.2, together

Table 7.2 Important nuclei for MRI and spectroscopy applications in vivo

Nucleus	Isotope	Natural abundance (%)	Magnetogyric ratio ($\times 10^7$ rad s^{-1} T^{-1})	Relative sensitivity (to ^{1}H)
Lithium	^{7}Li	92.4	10.398	6.52×10^{-4}
Carbon	^{13}C	1.07	6.728	1.76×10^{-4}
Fluorine	^{19}F	100	25.162	8.33×10^{-1}
Sodium	^{23}Na	100	7.081	9.27×10^{-2}
Phosphorus	^{31}P	100	10.839	6.65×10^{-2}

Note that all are *stable isotopes*. Imaging sensitivity is calculated by multiplying NMR sensitivity $\gamma^3 I(I+1)$ by natural abundance assuming for equimolar concentrations of each nucleus. To obtain imaging sensitivity, relative sensitivity must be scaled by expected tissue concentration

with indications of their relative sensitivity (relative to the proton used in conventional MRI), MRI characteristics, and natural abundance.

It is clear that all nuclei have lower sensitivity than the proton, although fluorine-19 has almost the same NMR sensitivity. The low sensitivity of these nuclei provide a challenge in terms of the concentration which must be present in the tissue for detection above background noise. Since MRI sensitivity depends on the concentration within the sampled region, one method to overcome low concentration is to simply sample much larger tissue volumes. (In proton MRI on high field animal scanners image pixels may represent tissue volumes of dimension 50 μm, whereas pixels for nuclei such as ^{31}P or ^{13}C will be several mm in dimension.) It is natural to then ask what is the attraction of working with such low sensitivity nuclei?

4.1.1 Spectroscopy Versus Imaging

The answer to this question lies in some of the earliest observations of the NMR phenomenon which underpin the field of chemical analysis by NMR. The Larmor frequency of a nucleus within a molecular environment is partially screened from the applied magnetic field by its electrons. The density of electrons associated with the nucleus depends on the nature of the chemical bond formed within the molecule, such that small variations in the Larmor frequency can be detected between differing molecular groups (known as the *chemical shift*). Using magnetic resonance spectroscopy (MRS) sequences the precessing magnetization is detected in the *absence* of any spatial encoding gradients allowing the frequency distribution due to chemical shift to be measured. Fourier transformation of the MRI signal now yields a *spectrum* rather than an image.

Carbon-13 has the advantage of low natural abundance which allows infusion of ^{13}C enriched compounds to be detected. Importantly metabolism of such infused compounds can be followed entirely non-invasively as breakdown of the original compound, and transfer of the ^{13}C atoms to other molecules can be seen via enhancement of the peaks at varying chemical shift [22–24]. Fluorine-19 and lithium (-6 or -7) have zero background concentration in vivo and so their detection can be uniquely attribute to infused labelled compounds or cells [25–27].

4.1.2   RF Systems for Non-proton Methods

From Table 7.2 we note that the magnetogyric ratio of each nuclei is different and so the Larmor frequency also varies with nucleus. MRI instrumentation must reflect these differences if nuclei other than proton are to be detected. The RF chain of the entire spectrometer—RF coils, RF amplifier and receiver—must be retuned to the new nucleus. Typically this requires the MRI spectrometer to be equipped with a second complete *broadband* RF system.

4.2   Hyperpolarization

In Sect. 3.1.1 it was noted that the strength of the MRI signal is determined by the bulk magnetization of the sample when placed in the main field B_o. Equation (7.8) showed that the number of nuclei in each available energy level is almost equal, even at very high static fields. Increasing the difference in occupancy in the energy levels can be achieved using the techniques of hyperpolarization which create large increases in magnetization and which have largely been applied to date in ^{13}C nuclei. Two broad categories of hyperpolarization method have been developed known respectively as dynamic nuclear polarization (DNP) and parahydrogen induced polarization (PHIP). These methods cannot be applied directly in vivo and as such require additional instrumentation to the basic MRI scanner, but they can however be used to increase the polarization of substrate compounds which can be injected into the animal as high sensitivity probes, in a analogous way to positron emission tomography (PET) probes.

4.2.1   Dynamic Nuclear Polarization (DNP)

The technique of dynamic nuclear polarization (DNP) enhances nuclear magnetization by transferring the polarization of the spin state of *unpaired electrons* into polarization of the nuclear spin states. Successful experiments using this technology for solution state NMR [28] and subsequently MRI [29] led to introduction of commercial instrumentation for DNP in 2005.

The DNP process is a complex multi-stage method. Initially the compound to be polarized is mixed with a trityl radical (as the source of unpaired electrons) and appropriate solvents such that the mixture will form a glass when frozen. The mixture is cooled in liquid helium under vacuum to less than 4 K, placed in a magnetic field (typically ~3.35 T) and irradiated with microwaves (typically at 94 GHz), which transfers electron polarization to the nucleus. Build-up of nuclear polarization occurs exponentially with a time constant of hundreds to thousands of seconds and consequently total irradiation time can be many hours to reach maximal polarization. When polarization is complete the sample is raised out of the helium bath but maintained in the magnetic field while it is rapidly thawed by injection of a pressurized hot solvent.

4.2.2 Parahydrogen

A full description of the technique of parahydrogen induced polarization is beyond the scope of this chapter and has been reviewed elsewhere [30]. However, a brief summary is worthwhile as an introduction to this subject. As we have noted above (Sect. 2.1) the proton has spin states α and β which are associated with the two energy levels of the nucleus when in the polarizing MRI field. Parahydrogen is a form of molecular hydrogen gas in which the two hydrogen nuclei have opposing spin states either αβ or βα. If a molecule of interest is subject to a hydrogenation reaction with parahydrogen, the resulting population of only certain energy levels of the resulting compound are significantly enhanced, leading to enhanced effective polarization of the sample. Parahydrogen is present naturally in molecular hydrogen at approximately 25 % at room temperature. The proportion of parahydrogen increases as the gas temperature is decreased (approximately 50 % of molecular gas is in the parahydrogen form at 77 K) but can also be significantly enhanced by passing the gas through a catalyst such as charcoal to prepare parahydrogen for reaction. Equipment and techniques for performing parahydrogen based MRI experiments of biomolecules have been described [31] and in vivo experiments have been performed [32]. While early experiments using parahydrogen required chemical hydrogenation of the biomolecule of interest, recent advances have shown that coordination of the biomolecule with parahydrogen via a catalyst but without direct chemical interaction can also achieve significant hyperpolarization [33]. These developing techniques of PHIP are simple, quick and cheaper to perform that DNP experiments, although no direct comparisons of efficiency are yet published.

In vivo applications of hyperpolarization techniques are still in their infancy but are being developed at a rapid pace and are already beginning to have a major impact on small animal molecular and cellular imaging studies by MRI.

5   Summary

The MRI spectrometer is a complex but highly versatile instrument offering the widest range of possibilities of all non-invasive scanning techniques. Many instrument configurations are possible depending on the precise nature of the imaging experiment to be conducted. The optimal configuration for any in vivo MRI measurement depends on careful selection of the most appropriate gradient and RF coil hardware.

References

1. Gadian DG (1996) NMR and Its Applications to Living Systems 2nd Edition ed: Oxford University Press.
2. McRobbie DW, Moore EA, Graves MJ, Prince MR (2007) MRI from picture to proton, 2nd Edition ed: Cambridge University Press.
3. Lauterbur PC (1973) Image Formation by Induced Local Interactions - Examples Employing Nuclear Magnetic-Resonance. Nature 242:190–191.
4. Bracewell RN (1999) The Fourier Transform & Its Applications 3rd Edition ed: McGraw-Hill Science/Engineering/Math.
5. Gifford WE, Longsworth RC (1964) Pulse tube refrigeration. Trans Am Soc Mec Eng 86: 264–268.
6. IEC (2002) Medical Electrical Equipment. Part 2–33. Particular requirements for basic safety and essential performance of magnetic resonance equipment for medical diagnosis., Vol. IEC 60601-2-33:2002. Geneva: International Electrotechnical Commission.
7. Romeo F, Hoult DI (1984) Magnet Field Profiling - Analysis and Correcting Coil Design. Magn Reson Med 1:44–65.
8. Mansfield P, Chapman B (1986) Active Magnetic Screening of Gradient Coils in NMR Imaging. J Magn Reson 66:573–576.
9. Gruetter R, Boesch C (1992) Fast, noniterative shimming of spatially localized signals - in vivo analysis of the magnetic-field along axes. J Magn Reson 96:323–334.
10. Gruetter R (1993) Automatic, localized in vivo adjustment of all 1st-order and 2nd-order shim coils. Magn Reson Med 29:804–811.
11. Blamire AM, Rothman DL, Nixon T (1996) Dynamic shim updating: A new approach towards optimized whole brain shimming. Magn Reson Med 36:159–165.
12. Zhao YS, Anderson AW, Gore JC (2005) Computer simulation studies of the effects of dynamic shimming on susceptibility artifacts in EPI at high field. J Magn Reson 173:10–22.
13. Haase A, Frahm J, Matthaei D, Hanicke W, Merboldt KD (1986) FLASH IMAGING - RAPID NMR IMAGING USING LOW FLIP-ANGLE PULSES. J Magn Reson 67:258–266.
14. Chen C-N, Hoult DI (1989) Biomedical magnetic resonance technology: IOP Publishing Limited.
15. Hayes CE, Edelstein WA, Schenck JF, Mueller OM, Eash M (1985) An Efficient, Highly Homogeneous Radiofrequency Coil for Whole-Body NMR Imaging at 1.5-T. J Magn Reson 63:622–628.
16. Axel L (1984) Surface Coil Magnetic-Resonance Imaging. J Comp Assist Tom 8:381–384.
17. Haase A, Hanicke W, Frahm J (1984) The Influence of Experimental Parameters in Surface-Coil NMR. J Magn Reson 56:401–412.
18. Roemer PB, Edelstein WA, Hayes CE, Souza SP, Mueller OM (1990) The NMR Phased-Array. Magn Reson Med 16:192–225.
19. Garbow JR, McIntosh C, Conradi MS (2008) Actively Decoupled Transmit-Receive Coil-Pair for Mouse Brain MRI. Concepts in Magnetic Resonance Part B-Magnetic Resonance Engineering 33B:252–259.
20. Mansfield P, Grannell PK (1973) NMR 'diffraction' in solids? J Phy C: Solid State Physics 6:L422-L426.
21. Ljunggren S (1983) A simple graphical representation of Fourier-based imaging methods. J Magn Reson 54:338–343.
22. Henry PG, Tkac I, Gruetter R (2003) H-1-localized broadband C-13 NMR spectroscopy of the rat brain in vivo at 9.4 T. Magn Reson Med 50:684–692.
23. Nabuurs C, Klomp DWJ, Veltien A, Kan HE, Heerschap A (2008) Localized sensitivity enhanced in vivo C-13 MRS to detect glucose metabolism in the mouse brain. Magn Reson Med 59:626–630.

24. van der Zijden JP, van Eijsden P, de Graaf RA, Dijkhuizen RM (2008) 1H/13C MR spectroscopic imaging of regionally specific metabolic alterations after experimental stroke. Brain 131:2209–19.
25. Procissi D, Claus F, Burgman P, Koziorowski J, Chapman JD, Thakur SB, et al. (2007) In vivo F-19 magnetic resonance spectroscopy and chemical shift imaging of tri-fluoro-nitroimidazole as a potential hypoxia reporter in solid tumors. Clin Cancer Res 13:3738–3747.
26. Srinivas M, Morel PA, Ernst LA, Laidlaw DH, Ahrens ET (2007) Fluorine-19 MRI for visualization and quantification of cell migration in a diabetes model. Magn Reson Med 58: 725–734.
27. van Heeswijk RB, Uffmann K, Comment A, Kurdzesau F, Perazzolo C, Cudalbu C, et al. (2009) Hyperpolarized Lithium-6 as a Sensor of Nanomolar Contrast Agents. Magn Reson Med 61:1489–1493.
28. Ardenkjaer-Larsen JH, Fridlund B, Gram A, Hansson G, Hansson L, Lerche MH, et al. (2003) Increase in signal-to-noise ratio of >10,000 times in liquid-state NMR. Proc Nat Acad Sci USA 100:10158–10163.
29. Golman K, Ardenaer-Larsen JH, Petersson JS, Mansson S, Leunbach I (2003) Molecular imaging with endogenous substances. Proc Nat Acad Sci USA 100:10435–10439.
30. Natterer J, Bargon J (1997) Parahydrogen induced polarization. Progress in Nuclear Magnetic Resonance Spectroscopy 31:293–315.
31. Hovener JB, Chekmenev EY, Harris KC, Perman WH, Robertson LW, Ross BD, et al. (2009) PASADENA hyperpolarization of C-13 biomolecules: equipment design and installation. Magnetic Resonance Materials in Physics Biology and Medicine 22:111–121.
32. Golman K, Axelsson O, Johannesson H, Mansson S, Olofsson C, Petersson JS (2001) Parahydrogen-induced polarization in imaging: Subsecond C-13 angiography. Magn Reson Med 46:1–5.
33. Adams RW, Aguilar JA, Atkinson KD, Cowley MJ, Elliott PIP, Duckett SB, et al. (2009) Reversible Interactions with para-Hydrogen Enhance NMR Sensitivity by Polarization Transfer. Science 323:1708–1711.